High-Strain, High-Strain-Rate Behavior of Tantalum

M.A. MEYERS, Y.-J. CHEN, F.D.S. MARQUIS, and D.S. KIM

Tantalum plate produced by a forging-rolling sequence was subjected to high plastic shear strains ($\gamma = 1 \rightarrow 5.5$) at high strain rates ($\sim 4 \times 10^4$ s^{-1}) in two experimental configurations: (a) a special hat-shaped geometry and (b) thin disks deformed in a split Hopkinson bar. In parallel experiments, the constitutive behavior of the same material was established through quasi-static and dynamic compression tests at ambient and elevated temperatures. The microstructure generated at high strain rates and retained by rapid cooling from a narrow (200-μm) deformation band progresses from dislocated, to elongated cells, to banded structures, and finally, to subgrains as the shear strain increases from 0 to 5.5. The temperature rise predictions from the constitutive description of the material indicate that the temperature reaches values of 800 K, and it is proposed that thermal energy is sufficient to produce a significant reorganization of the deformation substructure, leading to a recovered structure.

I. INTRODUCTION

IRON is the most common body-centered cubic (bcc) metal, and its mechanical behavior has been exhaustively studied. Tantalum has also received considerable attention; both exhibit a high temperature and strain-rate sensitivity, and their mechanical properties are strongly affected by interstitial solutions. Armstrong et al.[1] have attributed this behavior to the rate-controlling mechanism of the thermal component of the flow stress; whereas, in face-centered cubic (fcc) metals, the rate-controlling mechanism is the overcoming of dislocation forests by individual dislocations, it is considered to be the overcoming of Peierls–Nabarro stresses (through a ledgewise motion of dislocation kinks) for the bcc metals. A specific double-kink mechanism has been proposed by Seeger[2] and extended by Dorn and Rajnak.[3] Detailed analyses on thermally activated plastic deformation in tantalum have been carried out by Gypen and Deruyttere[4] (single crystals) and Werner[5] (solid solutions). Koizumi et al.[6] calculated the effect of the barrier shape on the flow stress *vs* temperature for a number of bcc metals, including tantalum. Anomalies in the flow stress decay with temperature were successfully correlated with barrier shape changes. It has been shown that the activation volume (or area) decreases with plastic strain for fcc metals and is constant for bcc metals. An increase in strain rate should only therefore produce a translation (upward or downward) of the stress-strain curve for bcc metals, whereas the work-hardening curves should "fan out" in fcc metals. The activation volume for bcc metals is much smaller than for fcc metals, yielding a much higher temperature and strain-rate sensitivity. This basic difference between the activation volumes of fcc and bcc metals has served as the basis for the Zerilli–Armstrong[7,8] constitutive equations.

The constitutive behavior of tantalum has been studied by Bechtold,[9] Gilbert et al.,[10] Mitchell and Spitzig,[11] Mordike and Rudolf,[12] and Hoge and Mukherjee.[13] More recently, the shock response of Ta has been explored by Lassila and Gray.[14] Gurevitch et al.[15] and Shih et al. [16] have reported evidence for recrystallization in recovered shaped-charge slugs and jets.

Tantalum is, because of its high density and ductility, an excellent material for use in shaped charges and explosively forged projectiles (EFPs). The plastic strains encountered in these applications are significant: up to 10 in shaped charges and up to 5 in EFPs. The objective of this study is to characterize the microstructural evolution and to understand the underlying mechanisms when tantalum is subjected to high strains at high strain rates.

II. MATERIAL AND EXPERIMENTAL METHODS

A. *Material*

The tantalum used in this investigation was produced and processed by Cabot Corp., Boyertown, PA. It was received as disks with a diameter of 155 mm and thickness of 8 mm. These disks were obtained through press forging of 30-cm-high ingots into 10-cm slabs. Subsequent to annealing, the slabs were cross-rolled to the final thickness (8 mm) with intermediate anneals. The final rolling direction was marked on each disk. As a result of processing, the disks exhibited a texture that was determined through direct pole figures and orientation distribution function analysis. Figure 1 shows the [100], [110], and [222] pole figures for the tantalum. The material clearly exhibits significant texture effects. The texture of tantalum is known to significantly affect the mechanical performance. Feng and Kumar[18] and Clark et al.[19,20] investigated the effects of processing parameters on texture. Clark et al.[19] state that cross-rolling is very effective in breaking up the as-cast columnar structure. It is also known that the performance of EFPs is critically dependent on their texture. The cross-rolling–annealing se-

M.A. MEYERS, Professor, Department of Applied Mechanics and Engineering Sciences, Y.-J. CHEN, Graduate Student, Institute for Mechanics and Materials, and D.S. KIM, Post-Doctoral Research Scientist, Center of Excellence for Advanced Materials, are with the University of California, San Diego, La Jolla, CA 92093. F.D.S. MARQUIS, Visiting Professor, is with the Institute for Mechanics and Materials, University of California, San Diego, and the Metallurgical Engineering Department, South Dakota School of Mines and Technology, Rapid City, SD 57701.

This article is based on a presentation made in the symposium "Dynamic Behavior of Materials," presented at the 1994 Fall Meeting of TMS/ASM in Rosemont, Illinois, October 3–5, 1994, under the auspices of the TMS-SMD Mechanical Metallurgy Committee and the ASM-MSD Flow and Fracture Committee.

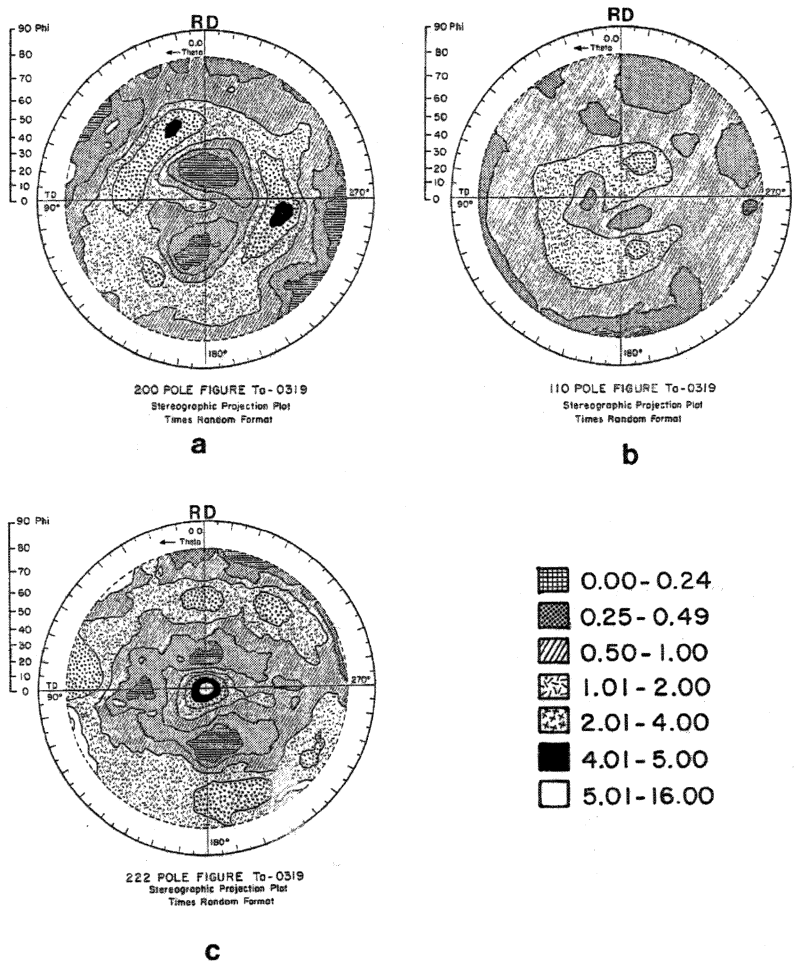

Fig. 1—Pole figures showing texture of as-received tantalum: numbers refer to times random (max: 5.85): (*a*) 200, (*b*) 110, and (*c*) 222; rolling direction for last pass marked RD.

quence led to an approximate grain size, as measured by the mean linear intercept, of 31 μm. Figure 2(a) shows the grain structure of the as-received material, while Figure 2(b) shows the dislocation structure. Some banding in the microstructure can be seen, due to uneven deformation/recrystallization. Two of these bands are marked in Figure 2(a). The dislocations generated in forging are not completely eliminated by the annealing treatments. The dislocation density shown in Figure 2(b) is $\sim 10^9$ cm^{-2}.

B. *Experimental Techniques*

The tantalum specimens were tested in compression and shear. Specimens were trepanned from the disks by electrodischarge machining. Compression specimens for quasistatic testing had dimensions of 4.83-mm diameter $\times$ 4.83-mm length. For dynamic testing, in a split Hopkinson bar, two types of specimens were tested: conventional compression specimens with 4.83-mm diameter $\times$ 3.81-mm length and especially designed specimens with 3-mm diameter $\times$ 0.4-mm thickness. The latter specimens were only used for recovery tests, since the frictional boundary conditions significantly affect the overall stress response. By the use of these thin specimens, it was possible to impart true effective compressive strains of up to -1.27.

Controlled shear experiments were carried out using the hat-shaped specimens developed by Meyer and Manwaring.[21] Hat-shaped specimens were used by Meyers et al.[22] for titanium and Andrade et al.[23,24] for copper. The technique is described in detail in these articles.[22,23,24] Controlled and prescribed levels of shear strain can be imparted, at high strain rates, in a region subjected to a state of simple shear. Figure 3(a) shows a schematic of loading the hat-shaped specimens in the Hopkinson bar before compression and the cross section of specimen with dimensions. The displacement was controlled by a special wave-trapping scheme developed by Nemat-Nasser et al.[25] The wave-trapping scheme presents two significant advantages: (a) it enables the establishment of prescribed and controlled shear strains; and (b) unwanted reflections, which can produce spurious straining of specimen, are eliminated. The strain rate was on the order of 4×10^4 s^{-1}. The average strain rate in the hat-shaped specimen is estimated by dividing the velocity of the incident bar, v, by the thickness of the plastic deformation region, L. This is equivalent to the strain per time. For a bar velocity (free surface velocity at specimen-incident bar interface) of 8 m/s and a band width of 200 μm, one obtains $\dot{\gamma} = v/L = 4 \times 10^4$ s^{-1}.

Dynamic compressive tests on cylindrical specimens were carried out at a strain rate of $\sim 3.5 \times 10^3$ s^{-1} at ambient and elevated temperatures (598 and 798 K). For the elevated tests, a furnace setup developed by Nemat-Nasser

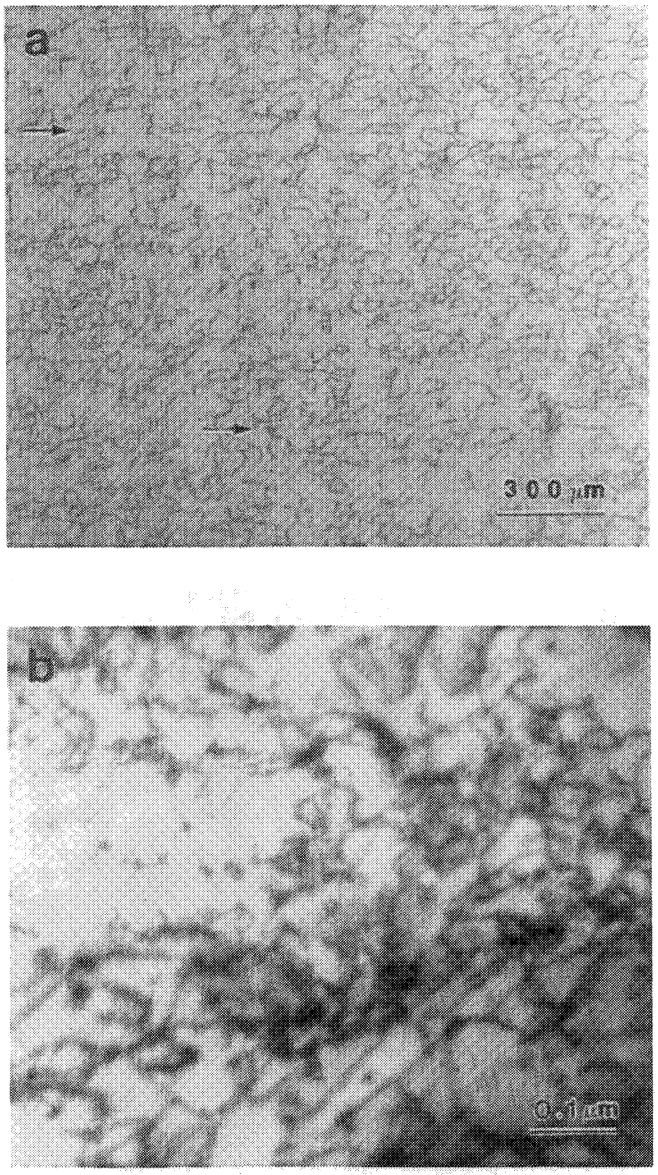

Fig. 2—Typical microstructure of the as-received tantalum: (*a*) grain structure showing banding and (*b*) transmission electron micrograph showing dislocation substructure.

et al.[25] was used. The high-strain-rate tests were carried out in two conditions: quasi-isothermal and adiabatic. Nemat-Nasser et al.[26] describe the method used to obtain quasi-isothermal stress-strain response under high-strain-rate deformation. It consists of carrying out incremental tests and allowing the specimen to return to the original testing temperature after each strain increment.

Hat-shaped specimens were sliced along the length of the deformation band (perpendicular to the specimen symmetry axis) for transmission electron microscopy (TEM). Typically, three to four slices were obtained. These slices were then polished and etched to reveal the evolution of the microstructure along the deformation band. Then, in one slice, typically three to four discs (ϕ = 3 mm) were cut for TEM from specific areas of precisely measured strain. Electropolishing (using a solution of 93 pct methanol + 5 pct sulfuric acid + 2 pct hydrofluoric acid at 233 K) was followed, where necessary, by ion milling.

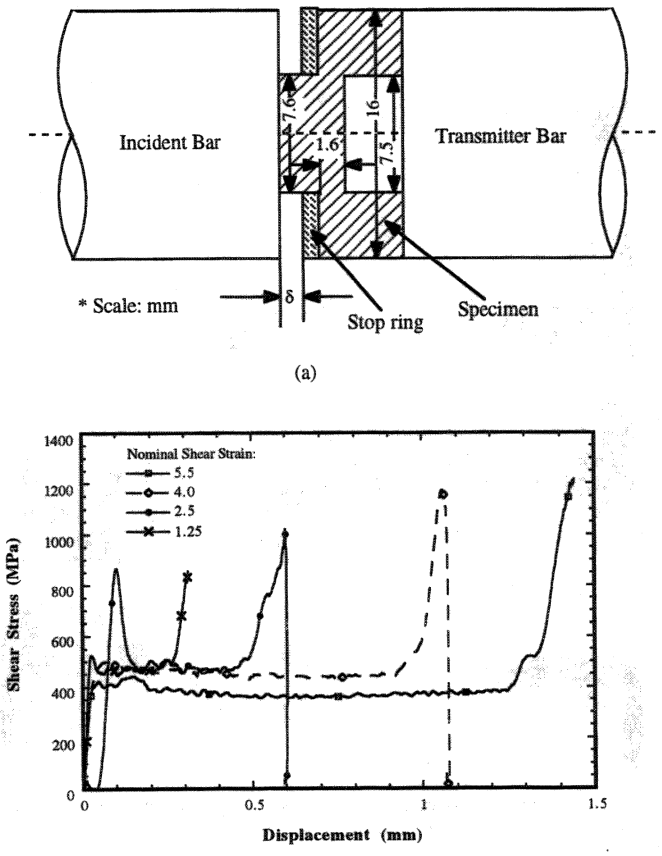

Fig. 3—(*a*) Schematic of loading of hat-shaped specimen in the Hopkinson bar before compression, and the cross section of specimen with dimensions. (*b*) Shear stress *vs* displacement of hat-shaped specimens.

III. RESULTS AND DISCUSSION

A. *Dynamic Shear Tests*

The objective of the experiments with the hat-shaped specimens was to probe the initiation of instability in the deformation or shear region. Figure 3(b) shows the shear-stress *vs* displacement curves obtained for four different prescribed displacements. The curves show a plateau at a shear-stress level of 400 to 500 MPa and a sharp increase when the prescribed displacement is reached, because a stopper ring was used to limit the displacement. Figure 4 shows the evolution of the microstructures along the shear localization regions for the different displacements, δ. The shear strains were estimated by two methods that provided similar results: by dividing the displacement by a approximate shear localization thickness, L (marked in Figure 4), and by measuring the deflection angle, α, of the shear markings (also marked in Figure 4). These methods are not very rigorous, since the thickness of the shear localization region is not constant and the shear varies with distance from the central area. Nevertheless, the agreement between the two measurements is a good indication of the reliability of the results. The first method was also applied to estimate the shear strain in each of the TEM discs. The shear strains are 1.25, 2.5, 4, and 5.5. Optical microscopy cannot reveal

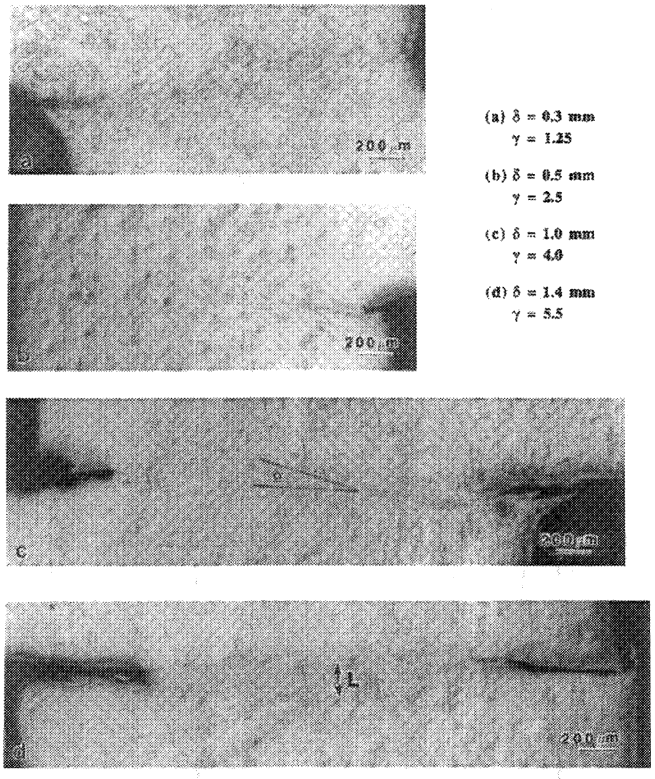

Fig. 4—Optical micrographs of shear localization regions: (*a*) $\gamma = 1.25$, (*b*) $\gamma = 2.5$, (*c*) $\gamma = 4.0$, and (*d*) $\gamma = 5.5$.

the details of the microstructural changes. They are presented in Section C. Figure 5 shows the distortion of the grains at shear-strain levels of (a) 1.25 and (b) 4. Plastic deformation is strongly inhomogeneous, some grains showing profuse slip markings, while others appear to be essentially strain free. In Figure 5(b), a region that apparently exhibits less plastic strain is marked by an arrow. The amount of shear also was observed to vary along the length of the shear localization region. This inhomogeneity manifests itself in differences in the residual microhardnesses, which are plotted in Figure 6(a) for $\gamma = 2.5$ and in (b) for $\gamma = 5.5$. Hardness profiles are shown for three positions along the shear band; they are indicated as top, middle, and bottom, respectively. For a displacement $\delta = 0.5$ mm ($\gamma = 2.5$), the hardness along the bottom traverse increases significantly more than along the other traverses. At the higher displacements, such as $\delta = 1.4$ mm ($\gamma = 5.5$), as shown in Figure 6(b), the differences have vanished. These differences are due to stress-strain concentrations at the sharp corners and variations in the band thicknesses, which can also be seen in Figure 4. These results indicate that fluctuations in shear strain occur along the length of the shear localization region; the shear-strain values given in Figure 4 are only average values. This can be responsible for the marked differences in deformation structures observed by TEM (Section C).

B. *Constitutive Description of Process*

The thermal excursion undergone by the deforming material, at the high strain rates imposed, is a function of the strain rate. At the strain rate of 4×10^4 s^{-1}, the process

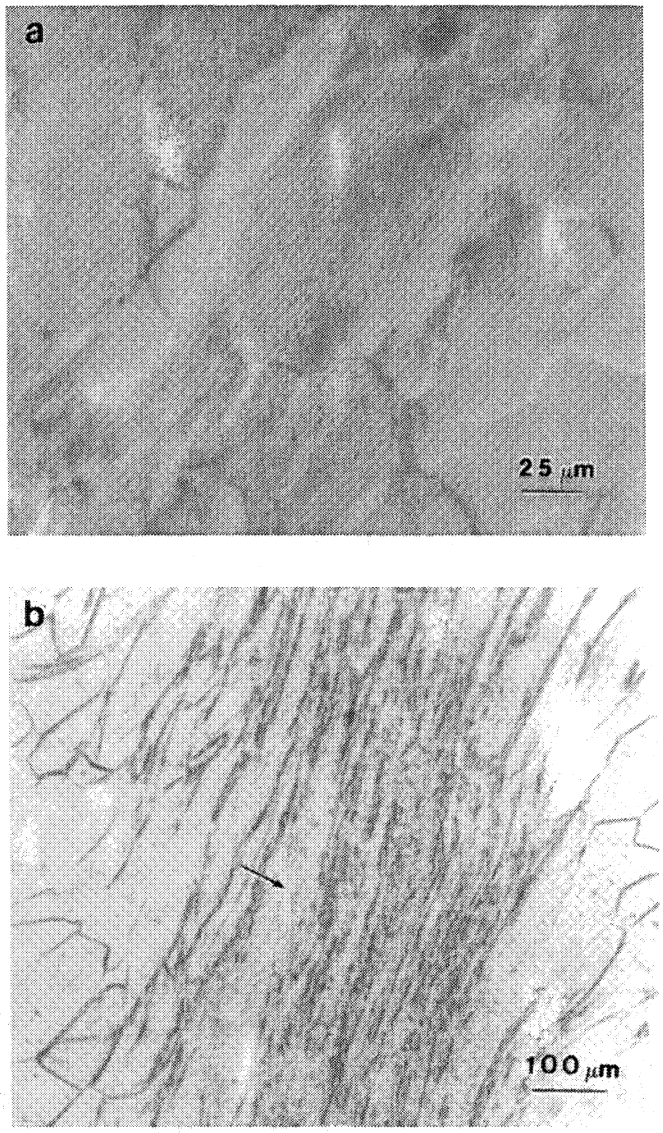

Fig. 5—Shear localization region for (*a*) $\gamma = 1.25$ and (*b*) $\gamma = 4$. Microstructure of the region within shear deformation shows strong inhomogeneous plastic deformation and banding within selected grains.

can be considered essentially adiabatic, since the thermal diffusion length, L, is approximately given by

$$L \cong 2(\alpha t)^{1/2}$$

Here α is the thermal diffusivity, and t is the deformation time. The critical strain rate can be defined as

$$\dot{\varepsilon}_{cr} \cong \frac{4\alpha\varepsilon}{L^2}$$

If one considers L to be the thickness of the shear localization region in the hat-shaped specimen ($L \sim 0.2$ mm), the critical strain rate for these conditions ($\alpha_{Ta} = 0.29$ cm^2/s) is approximately 3×10^3 s^{-1} at $\varepsilon = 1$. Thus, the process can be assumed to be adiabatic. In order to determine the temperature evolution under high-strain-rate deformation, compression tests in cylindrical specimens were carried out at different temperatures and strain rates; the resulting data were used to determine the parameters of a modified Johnson–Cook[27,28] constitutive equation, which

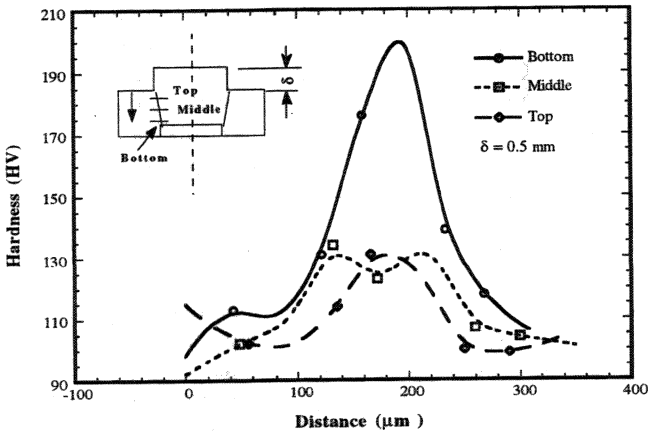

(a)

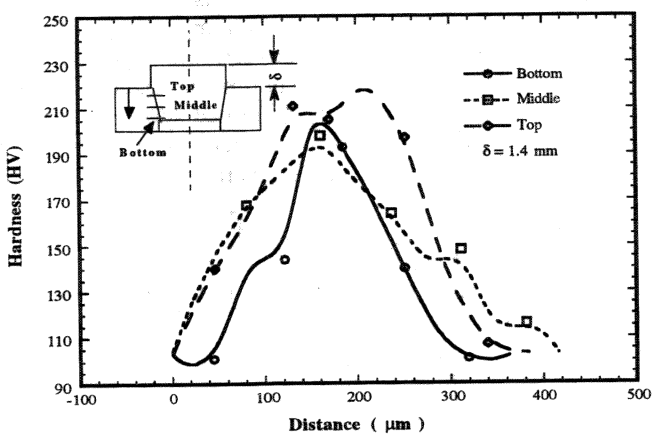

(b)

Fig. 6—Microindentation hardness as a function of distance along sheared cross section. (*a*) Prescribed displacement: 0.5 mm and (*b*) prescribed displacement: 1.4 mm.

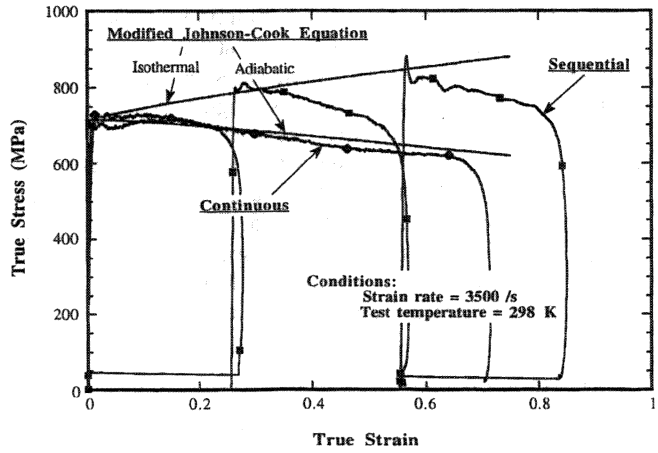

Fig. 7—Continuous and sequential (isothermal) stress-strain response of tantalum at nominal strain rate of 3500 s^{-1} in room temperature.

enabled the prediction of temperature as a function of plastic strain.

The use of interrupted tests in the Hopkinson bar, as

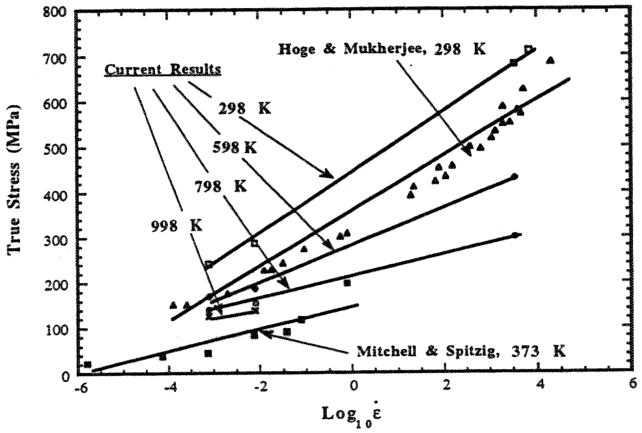

(a)

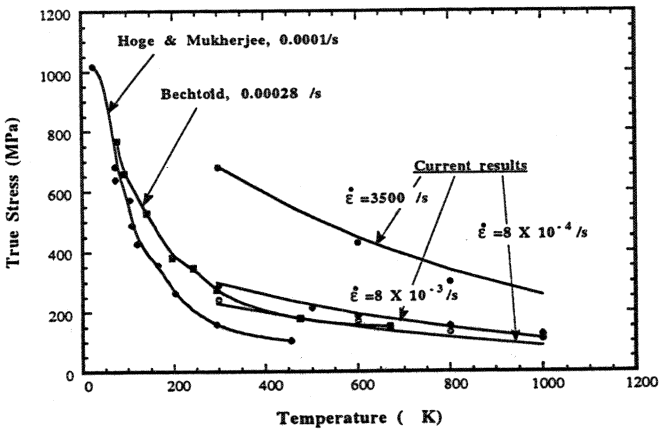

(b)

Fig. 8—(*a*) Strain-rate and (*b*) temperature dependence of flow stress for tantalum.

developed by Nemat-Nasser et al.,[25] enabled the establishment of the isothermal curve. These tests had been previously used by Wittman et al.[29]. This is illustrated in Figure 7. The results of a compression test, carried out to a true plastic strain of −0.73 at a strain rate of 3.5×10^3 s^{-1}, are compared with those of three sequential tests, carried out on the same specimen by sequentially reloading it. The origins of the second and third tests were translated so that the strain is additive. The specimen was allowed to cool down prior to the second and third tests. The stress-strain curves show the hardening that is masked by thermal softening in the single test. The envelope of the sequential tests defines an isothermal curve, which diverges significantly from the adiabatic curve. Adiabatic deformation yields softening beyond the strain of 0.1. The strain-rate dependence of the flow stress was determined from the results shown in Figure 8(a). The results of tests carried out at 298, 598, and 798 K are compared with earlier results by Mitchell and Spitzig[11] and Hoge and Mukherjee.[13] The current research only used three strain rates, but the strain-rate dependence is very similar. Another characteristic of the tantalum in the present investigation is its high yield stress,

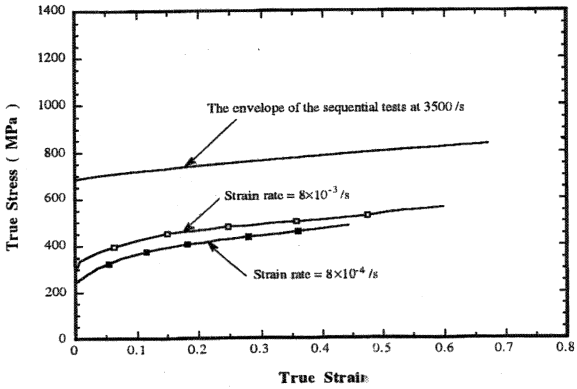

(a)

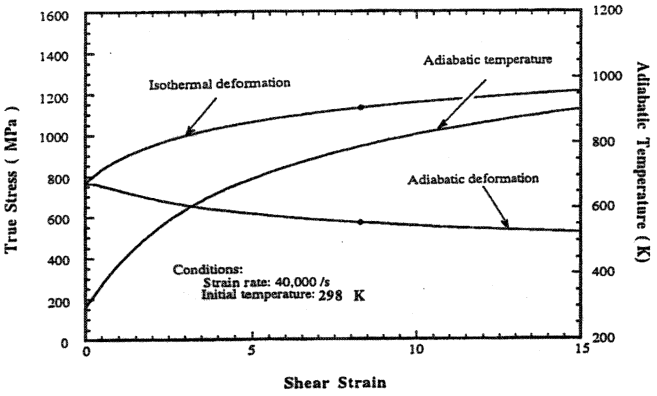

(b)

Fig. 9—(*a*) Comparison of stress-strain curves at different strain rates. (*b*) Calculated flow stress and adiabatic temperature as a function of strain for different strain rates, at 4×10^4 s^{-1}.

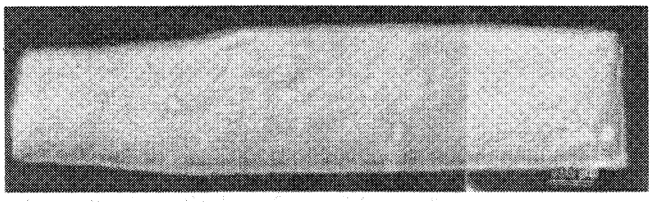

Fig. 10—Cross section of cylindrical tantalum specimen deformed in compression at 3.5×10^3 s^{-1}, to a maximum plastic strain of −0.7.

consistently with the high dislocation density observed in the as-received material (Figure 2). The effect of temperature on the yield stress is shown in Figure 8(b); the behavior is consistent with results by Hoge and Mukherjee[13] and Bechtold.[9] The yield stress is considerably higher than that observed by these investigators, a direct result of the hardened condition of the material. These tests were used to obtain the parameters necessary in the Johnson–Cook equation,[27,28] which had a modified thermal softening term:

$$\sigma = (\sigma_0 + B\varepsilon^n)\left[1 + C\left(\log_{10}\frac{\dot{\varepsilon}}{\dot{\varepsilon}_0}\right)\right]e^{-\lambda(T-T_r)} \qquad [1]$$

where σ_0 is the yield stress, B and n are work-hardening terms, C describes the strain-rate sensitivity, and λ parametrizes the thermal softening. A straight line was assumed for the strain-rate response in Figure 8(a). The parameters σ_0, B, n, and λ were obtained from the tests conducted at a reference strain rate and a reference temperature, T_r. The Johnson–Cook equation[27,28] is not very successful in representing the effect of strain rate on work hardening for bcc metals because the three components (work hardening, thermal strain-rate hardening, and thermal softening) are multiplied in Eq. [1], whereas the stress-strain curves are merely translated along the stress axis for tantalum. This can be seen in Figure 9(a), where the isothermal stress-strain curve at 3.5×10^3 s^{-1} is compared with the curves at 8×10^{-4} and 8×10^{-3} s^{-1}. The parallelism between the curves is a direct result of the rate-controlling mechanism of plastic deformation for bcc metals: the thermally activated motion of the kinks along dislocations. The activation volume for this is not affected by plastic strain, and therefore the evolution of hardening is insensitive to strain rate. The following values were obtained: $\sigma_0 = 684.5$ MPa: $B = 205.3$ MPa: $n = 0.78$: $C = 0.1$: $\dot{\varepsilon}_0 = 3500$/s: $T_r = 298$ K: and $\gamma = 0.0014$.

The reference strain rate was taken as 3500/s in order to provide a more reliable prediction of temperature evolution, because of the differences between the Johnson–Cook equation[27,28] and the actual experimental data. The temperature rise of the plastically deformed specimen was estimated by assuming a conversion factor of work into heat of 0.9 (T_0 is the initial testing temperature):

$$\int_{T_0}^{T} \rho C_p dT = 0.9 \int_0^{\varepsilon} \sigma d\varepsilon \qquad [2]$$

From Eqs. [1] and [2], the temperature can be expressed as a function of strain, ε:

$$T = T_r + \frac{1}{\lambda} Ln\left[e^{\lambda(T_0 - T_r)} + 0.9\lambda \frac{1 + C\left(\log_{10}\frac{\dot{\varepsilon}}{\dot{\varepsilon}_0}\right)}{\rho C_p} \varepsilon\left(\sigma_0 + \frac{B}{n+1}\varepsilon^n\right)\right] \qquad [3]$$

The predicted temperature as a function of plastic shear strain is plotted in Figure 9(b) for a strain rate of 4×10^4 s^{-1}. This is the strain rate within the shear localization region in the hat-shaped specimens. Figure 9(b) also shows the isothermal and adiabatic stress-strain curves. The two curves change, in accordance with the experimental results of Figure 7. The highest shear strain imparted to the hat-shaped specimens was equal to 5.5. The plastic strains in the hat-shaped and disk-shaped specimens can be compared if an equivalent strain is calculated. For the shear strain $\gamma = 5.5$, the temperature reaches a value of 800 K.

C. *Evolution of Microstructure*

The effect of increased plastic strain, at the strain rates imposed by dynamic tests, will be discussed in this section. Macroscopically, no localization was observed in the cylindrical compression specimens tested at 3.5×10^3 s^{-1}. Figure 10 shows the cross section of a specimen that received a compressive strain of −0.7. The corresponding stress-strain curve is shown in Figure 7. The absence of shear localization, in spite of the unstable stress-strain curve, is

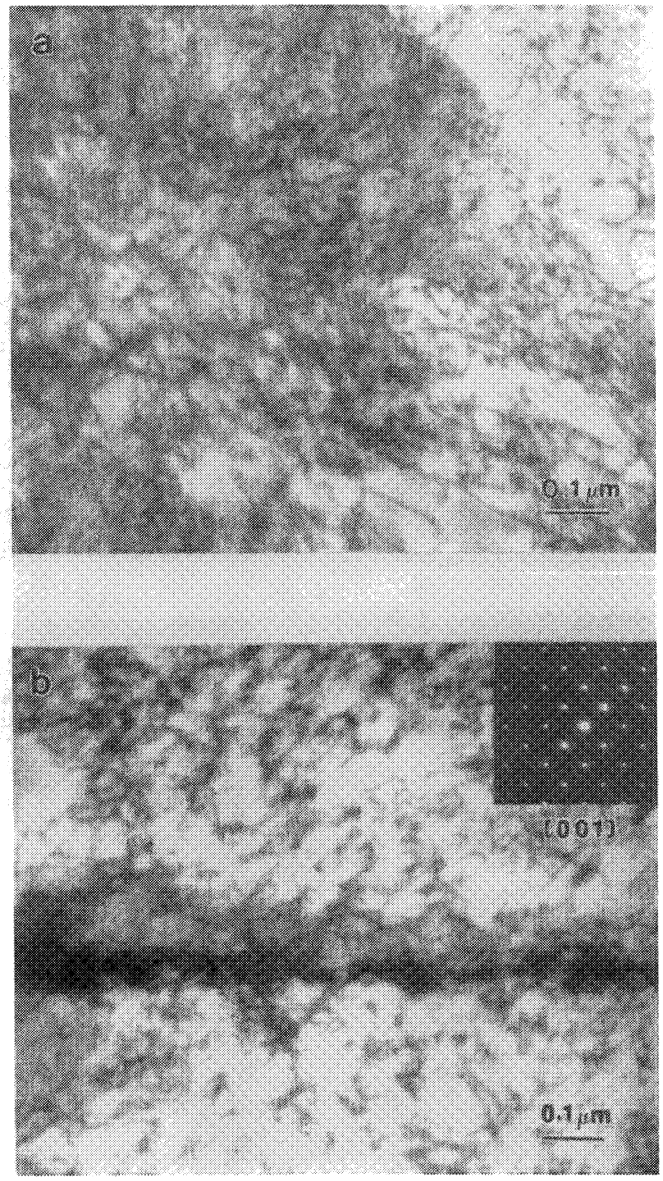

Fig. 11—Transmission electron micrographs from disk-shaped specimen deformed to strains $\varepsilon_{eff} = 0.69$ and $\varepsilon_{eff} = 1.27$, at a strain rate of 4×10^4 s^{-1}: (*a*) $\varepsilon_{eff} = 0.69$, homogeneous dislocation distribution and (*b*) $\varepsilon_{eff} = 1.27$, incipient bands.

consistent with earlier results by Meyers et al.[22] for titanium. They observed that unstable plastic flow (i.e., a negative slope in the stress-strain curve) preceded shear localization by a significant amount. Wright[30,31] developed a theoretical framework according to which localization and instability are separate phenomena. Meyers et al.[22] provided a microstructural interpretation in terms of dynamic recrystallization; they suggested that instability is produced by the increase of thermal assistance to the motion of dislocations, whereas localization requires dynamic recovery/recrystallization. The melting point of tantalum is 3000 K. If one considers, to a first approximation, that the onset of dynamic recrystallization occurs at $0.4T_m$, one obtains a value of 1200 K. Recrystallization temperature is known to be a function of plastic strain.[32] The value for recrystallization temperature given by Köck and Paschen[33] is 1200 to 1500 K, slightly higher than the $0.4T_m$ estimate. On the

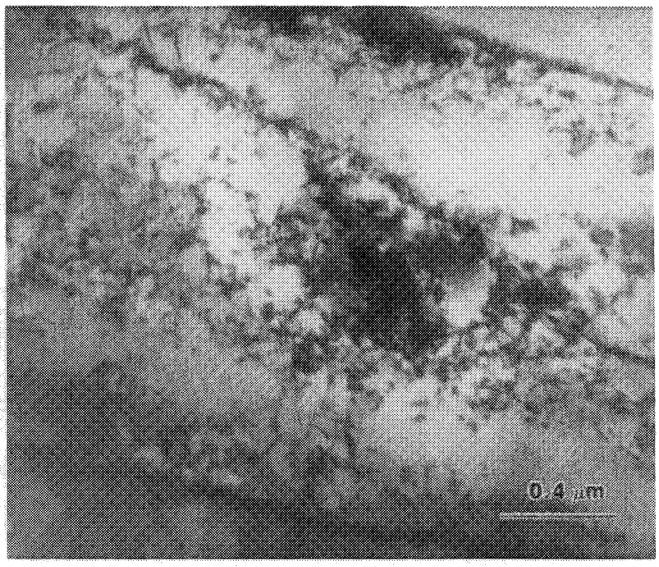

Fig. 12—Transmission electron micrograph from hat-shaped specimen deformed to $\gamma = 1.25$ ($\varepsilon_{eff} = 0.72$).

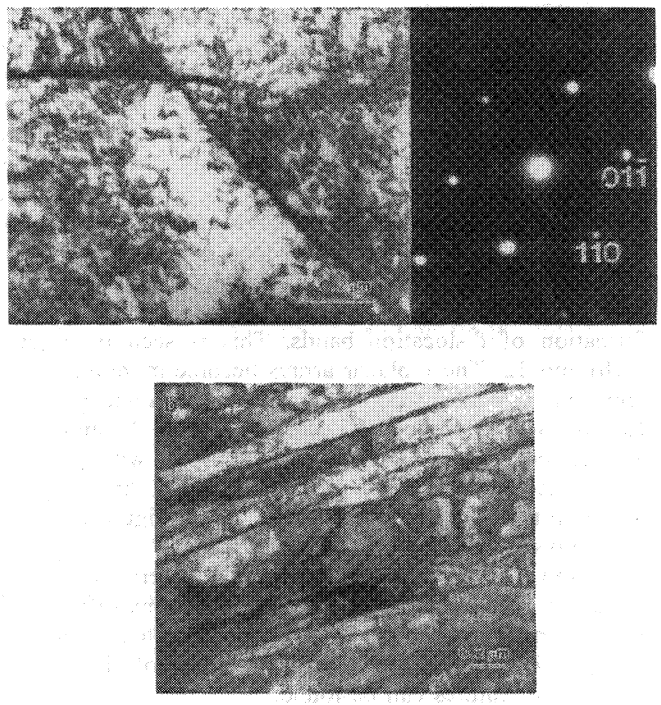

Fig. 13—Transmission electron micrograph from hat-shaped specimen deformed to $\gamma = 2.5$ ($\varepsilon_{eff} = 1.44$): (*a*) intersecting bands and (*b*) arrays of elongated cells.

other hand, recent experiments by Beckenhauer et al.[34] yielded a recrystallization temperature in high-purity Ta of 1003 K. This was accomplished by heating the specimen at 830 K/s, which inhibited recovery processes because of its rapidity. This value can be taken as a lower bound for dynamic recrystallization in tantalum. From the predicted temperature *vs* shear-strain plot of Figure 9(b), a shear strain higher than 15 would be required for the process.

The results of TEM observations of selected specimens are presented in Figures 11 through 16 and are consistent with the aforementioned temperature estimates. The microstructures observed in the hat-shaped and disk-shaped

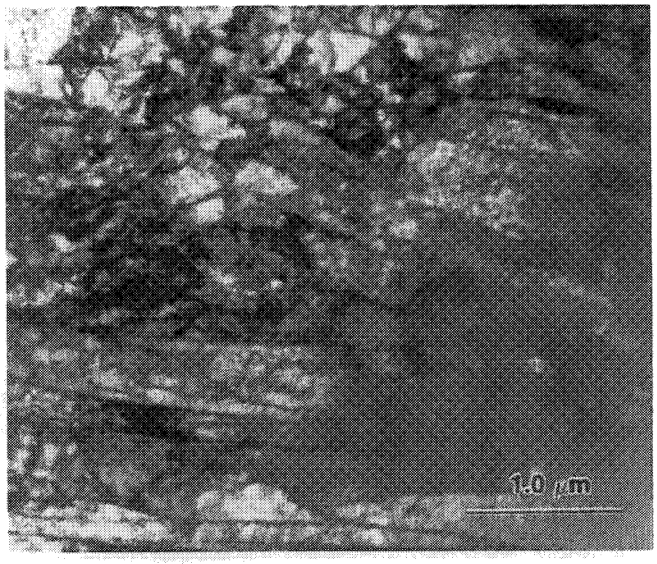

Fig. 14—Transmission electron micrograph from hat-shaped specimen deformed to $\gamma = 5.5$ ($\varepsilon_{eff} = 3.18$).

specimens are consistent, the principal advantage of the latter being the ease of specimen preparation because of the large amount of deformed material produced in each test. Effective strains will be used in the discussion, in order to enable comparison between the two methods. As the plastic strain is increased, the dislocation density correspondingly increases. Figure 11(a) shows the microstructure of the disk-shaped specimen at an effective strain of $\varepsilon_{eff} = 0.69$. The dislocation density is higher than the as-received condition (Figure 2(b)). At higher effective strains, such as $\varepsilon_{eff} = 1.27$, the dislocation density increases further, with the formation of dislocation bands. This is seen in Figures 11(b) and 12. These planar arrays become more and more prevalent as plastic strain is increased, as shown in Figure 13. At shear strains of 2.5 and 4 ($\varepsilon_{eff} = 1.44$ and 2.31, respectively), the slip bands form a network with intersections. These bands are oriented along ⟨110⟩ directions, as shown in the electron diffraction pattern of Figure 13. Similar arrays were observed by Murr et al.,[35] Worsick et al.,[36] and Wittman et al.[37] reported the observation of deformation twins, but this is not substantiated by diffraction. These bands have an approximate spacing that decreases with plastic strain. In the optical micrograph of Figure 5(a), these same features can be found.

As the plastic shear strain is increased to 4 and 5.5, the dislocations tend to form better and better defined cells, which progressively become subgrains. In some cases, they form along different orientations (Figure 14), while in other cases they are elongated along one orientation (Figure 15). This subgrain morphology is identical to that observed by Murr et al.[17] These features are also similar to the ones observed by Mgbokwere et al.[38] for an AISI 4340 steel. It is proposed that these subgrains are formed by a dynamic recovery mechanism, enabled by the thermal excursion that results from the conversion of plastic work into heat.

There is evidence that isolated regions underwent the first stages of dynamic recrystallization. Several factors can contribute to this: (a) the plastic shear strain is not uniform along the length of the shear localization region; and (b) the plastic strain varies from grain to grain, leading to

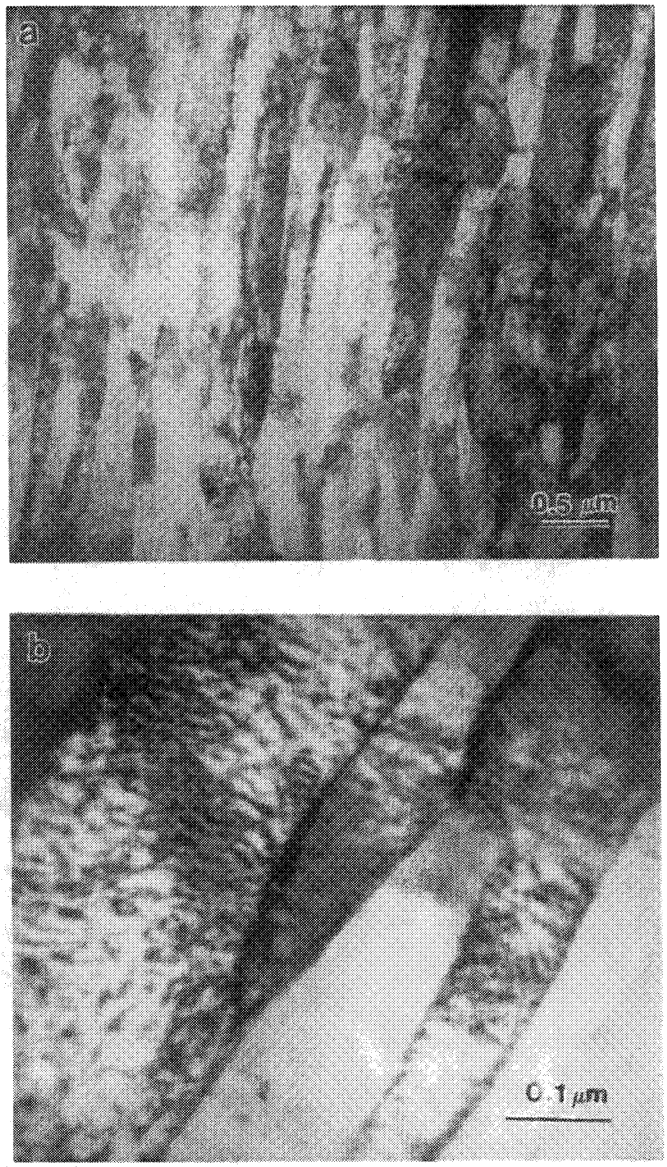

Fig. 15—Transmission electron micrograph from hat-shaped specimen deformed to $\gamma = 5.5$ ($\varepsilon_{eff} = 3.18$) at 4×10^4 s^{-1} (notice pronounced subgrain formation): (*a*) lower magnification and (*b*) higher magnification.

regions that undergo higher deformation than the average. Typical examples of both factors are shown in Figures 5(a) and (b) and 6(a) and (b). One of these regions is shown in Figure 16. The breakup of the existing microstructures with well-defined interfaces and the reflections from the diffraction pattern forming a circle seem to indicate a more drastic process than dynamic recovery. Dynamic recrystallization has been proposed by Murr et al.[35] and Gurevitch et al.[15] to play an important role in shaped-charge deformation. Indeed, they have characterized recovered specimens from jets and slugs and concluded that dynamic recrystallization occurred during jet elongation.

IV. CONCLUSIONS

The principal conclusions that were obtained from the research program are as follows:

1. A hat-shaped specimen and a thin disk-shaped specimen

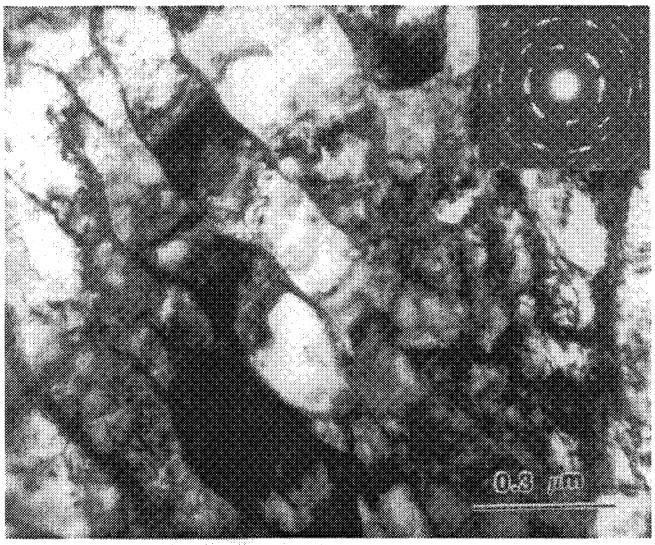

Fig. 16—Early stages of dynamic recrystallization.

were used to investigate the microstructural evolution at high strains and strain rates, in tantalum. Both geometries enable controlled and prescribed plastic deformations, at strain rates on the order of 4×10^4 s^{-1}, and a rapid subsequent cooling of the deformed zone because of the small dimensions of the deformation region (~200 μm). This ensures the retention of the deformation substructure in the recovered specimens.

2. Shear strains up to 5.5 were accomplished, and separate experiments coupled with the application of a constitutive equation led to temperature predictions as a function of plastic deformation.
3. The microstructure generated at high strain rates evolves from a high density of uniformly distributed dislocations, to slip bands and their intersections, to subgrains. For the highest shear strain imparted in the current experiments, the temperature reaches a predicted value of 800 K, below the critical value for dynamic recrystallization (1000 to 1200 K).
4. In isolated regions, typically at high microscopic strains, the onset of dynamic recrystallization was observed.

ACKNOWLEDGMENTS

This research was funded by the United States Army Research Office through the University Research Initiative Program (Contract No. DAAL03-92-G0108). Partial support for F.D.S. Marquis and Y.-J. Chen was also obtained through the Institute for Mechanics and Materials. The authors would like to express their appreciation to S. Nemat-Nasser and K.S. Vecchio for stimulating discussions and to J.B. Isaacs for carrying out part of the Hopkinson bar experiments. The material for research was kindly provided by Dr. W. Ebihara and Mr. M. Hespos, ARDEC.

REFERENCES

1. R.W. Armstrong, V. Ramachandran, and F.J. Zerilli: in *Advances in Materials and Their Applications*, P. Rama Rao, ed., Wiley Eastern Ltd., New Delhi, 1988, p. 201.
2. A. Seeger: *Phil. Mag.*, 1956, vol. 1, pp. 651-62.
3. J.E. Dorn and S. Rajnak: *Trans. AIME*, 1964, vol. 230, pp. 1052-64.
4. L.A. Gypen and A. Deruyttere: *J. Less-Common Met.*, 1982, vol. 86, pp. 219-40.
5. M. Werner: *Phys. Status Solidi*, 1987, vol. 104, pp. 63-78.
6. H. Koizumi, H.O.K. Kirchner, and T. Suzuki: *Acta Metall. Mater.*, 1993, vol. 41, pp. 3483-93.
7. F.J. Zerilli and R.W. Armstrong: *J. Appl. Phys.*, 1986, vol. 61, pp. 1816-25.
8. F.J. Zerilli and R.W. Armstrong: *J. Appl. Phys.*, 1990, vol. 68, pp. 1580-91.
9. J.H. Bechtold: *Acta Metall.*, 1955, vol. 3, pp. 249-54.
10. A. Gilbert, D. Hull, W.S. Owen, and C.N. Reid: *J. Less-Common Met.*, 1962, vol. 4, pp. 399-408.
11. T.E. Mitchell and W.A. Spitzig: *Acta Metall.*, 1965, vol. 13, pp. 1169-79.
12. B.L. Mordike and G. Rudolf: *J. Mater. Sci.*, 1967, vol. 2, pp. 332-38.
13. K.G. Hoge and A.K. Mukherjee: *J. Mater. Sci.*, 1977, vol. 12, pp. 1666-72.
14. D. Lassila and G.T. Gray III: *J. Phys., Colloq.*, 1991, vol. 1, pp. 19-26.
15. A.C. Gurevitch, L.E. Murr, H.K. Shih, C.-S. Niou, A.H. Advani, D. Manuel, and L. Zernow: *Mater. Charact.*, 1993, vol. 30, pp. 201-16.
16. H.K. Shih, L.E. Murr, C.-S. Niou, and L. Zernow: *Scripta. Metall. Mater.*, 1993, vol. 29, pp. 1291-96.
17. L.E. Murr, H.K. Shih, and C.-S. Niou: *Mater. Charact.*, 1994, vol. 33, pp. 65-74.
18. C. Feng and P. Kumar: *J. Met.*, 1989, vol. 41, pp. 40-45.
19. J.B. Clark, R.K. Garrett, Jr., T.L. Jungling, R.A. Vandermeer, and C.L. Vold: *Metall. Trans. A*, 1991, vol. 22A, pp. 2039-48.
20. J.B. Clark, R.K. Garrett, T.L. Jungling, and R.I. Asfahani: *Metall. Trans. A*, 1992, vol. 23A, pp. 2183-91.
21. L.W. Meyer and S. Manwaring: in *Metallurgical Applications of Shock-Wave and High-Strain-Rate Phenomena*, L.E. Murr, K.P. Staudhammer, and M.A. Meyers, eds., Marcel Dekker, New York, NY, 1986, p. 657.
22. M.A. Meyers, G. Subhash, B.K. Kad, and L. Prasad: *Mech. Mater.*, 1994, vol. 17, pp. 175-99.
23. U.R. Andrade, M.A. Meyers, K.S. Vecchio, and A.H. Chokshi: *Acta Metall. Mater.*, 1994, vol. 42, pp. 3183-95.
24. M.A. Meyers, U.R. Andrade, and A.H. Chokshi: *Metall. Mater. Trans.*, in press.
25. S. Nemat-Nasser, J.B. Isaacs, and J.E. Starrett: *Proc. R. Soc. London A*, 1991, vol. A20, pp. 371-91.
26. S. Nemat-Nasser, Y.-F. Li, and J.B. Isaacs: *Mech. Mater.*, 1994, vol. 17, pp. 111-34.
27. G.R. Johnson and W.H. Cook: in *Proc. 7th Int. Symp. on Ballistics*, The Hague, The Netherlands, 1983, pp. 1-7.
28. G.R. Johnson and T.J. Holmquist: *J. Appl. Phys.*, 1988, vol. 64, pp. 3901-10.
29. C.L. Wittman, C.M. Lopatin, J.P. Swensen, and T.J. Holmquist: in *High Strain Rate Behavior of Refractory Metals and Alloys*, R. Asfahani, E. Chen, and A. Crowson, eds., TMS-AIME, Warrendale, PA, 1992, pp. 167-78.
30. T.W. Wright: *J. Mech. Phys. Solids*, 1990, vol. 38, pp. 515-30.
31. T.W. Wright: *Mech. Mater.*, 1994, vol. 17, pp. 215-22.
32. R.E. Reed-Hill: *Physical Metallurgy Principles*, 2nd ed., PWS Engineering, Boston, MA, 1973, pp. 284-90.
33. W. Köck and P. Paschen: *J Met.*, 1989, vol. 41 (10), pp. 33-39.
34. D. Beckenhauer, P. Niessen, and P. Pick: *J. Mater. Sci. Lett.*, 1993, vol. 12, pp. 449-50.
35. L.E. Murr, C.-S. Niou, and C. Feng: *Scripta Metall. Mater.*, 1994, vol. 31, pp. 297-302.
36. M.J. Worswick, N. Qiang, P. Niessen, and R.J. Pick: in *Shock-Wave and High-Strain-Rate Phenomena in Materials*, M.A. Meyers, L.E. Murr, and K.P. Staudhammer, eds., Marcel Dekker, New York, NY, 1992, pp. 87-95.
37. C.L. Wittman, R.K. Garrett, J.B. Clark, and C.M. Lopatin: in *Shock-Wave and High-Strain-Rate Phenomena in Materials*, M.A. Meyers, L.E. Murr, and K.P. Staudhammer, eds., Marcel Dekker, New York, NY, 1992, pp. 925-33.
38. C.O. Mgbokwere, S.R. Nutt, and J. Duffy: *Mech. Mater.*, 1994, vol. 17, pp. 97-110.